Hindawi
Journal of Nanomaterials
Volume 2022, Article ID 5675038, 13 pages
https://doi.org/10.1155/2022/5675038

Research Article

The Tribological Behavior of Nanocrystalline TiO_2 Coating Produced by Plasma Electrolytic Oxidation

S. Abbasi,[1] A. Mahboob,[2] H. Bakhtiari Zamani,[3] M. R. Bilesan,[4] E. Repo,[4] and A. Hakimi[5]

[1]*School of Mechanical, Industrial and Manufacturing Engineering, Oregon State University, Corvallis, OR 97330, USA*
[2]*Strength of Materials and Structural Engineering Department, Polytechnic University of Catalonia, C/Colom 11, TR45, 08222 Terrassa, Spain*
[3]*Advanced Materials Research Center, Department of Materials Engineering, Najafabad Branch, Islamic Azad University, Najafabad, Iran*
[4]*Department of Separation Science, LUT School of Engineering Science, LUT University, FI-53850 Lappeenranta, Finland*
[5]*Department of Pharmacology, Ghalib University, West of Park Taraqi, Hanzala Badghisi Road, Herat, Afghanistan*

Correspondence should be addressed to A. Hakimi; abdulqaiyoum.hakimi@gmail.com

Received 2 October 2021; Accepted 20 December 2021; Published 17 January 2022

Academic Editor: Pingan Song

Nanocrystalline TiO_2 coatings were produced on titanium substrates using the plasma electrolytic oxidation technique. The effects of frequency, duty cycle, and type of applied current (pulse and direct) were evaluated on the microstructure of the coatings and the tribological behavior of the samples. Morphological evaluations demonstrated that the pancake structure was developed from coatings created with a unipolar pulsed current. However, a volcano-like surface morphology resulted from a constant current. The XRD analysis results showed that the coatings were composed mainly of the rutile phase by 77.80-96.34 wt. %. In comparison, 22.20 wt. % of the anatase phase was identified in samples produced with direct current. These phases were determined to be nanocrystalline (29.5-48.3 nm), which led to significant improvements in the tribological properties. The sample produced with direct current had larger pores, greater roughness, and a four-times higher thickness than samples created with unipolar current. Furthermore, the tribological study results showed that wear resistance was significantly higher in the unipolar pulsed current coatings than in those obtained with direct current. Moreover, samples made at a higher frequency and lower duty cycle showed better tribological behavior.

1. Introduction

Pure titanium (Ti) and titanium alloys have been extensively used in the aerospace, automotive, marine, medical, and energy industries. Ti and its alloys have some desirable properties, including low density, low elastic modulus, high strength-to-weight ratio, high melting point, and great biocompatibility, as well as good corrosion, creep, and fatigue resistance [1, 2]. However, Ti has some disadvantages, including high friction coefficient, low abrasive, low adhesive wear resistance (weak tribological properties) [3–5].

To increase the Ti wear resistance, TiO2 is commonly used as a covering. To deposit TiO2 coating on the Ti surface, various surface modifying techniques classified as physical, chemical, and electrochemical methods have been used [6–8]. The newest electrochemical coating process is generally known as plasma electrolytic oxidation (PEO) [9, 10].

The PEO process is typically affected by many intrinsic and extrinsic variables. Extrinsic variables are related to electrical parameters. Substance and electrolyte composition as intrinsic variables substantially affect the microstructure and composition of coatings. Some other variables, such as processing time, electrolyte temperature, and additives, influence the coatings' morphology and roughness [11–14].

Various types of electric current are used in the PEO process. Direct current can provide constant current and voltage. However, this source cannot fully control PEO due to its difficulty in regulating the current during the electrical discharge occurrence. Therefore, direct current is typically used to apply thin coatings on metal substrates with a simple

Table 1: Chemical composition of the CP-grade II Ti substrate was used in this research.

Elements	Al	V	Cr	Cu	Fe	Mn	Mo	Nb	Sn	Zr	Ti
Wt. %	0.01	0.05	0.01	0.02	0.07	0.03	0.03	0.01	0.05	0.01	Bal.

Table 2: The parameters of different coating processes on Ti.

Sample	Current type	Current density ($mA.Cm^{-2}$)	Frequency (Hz)	Duty cycle (%)	Coating time (min)	Ultimate voltage (V)	Sparking time (s)	Sparking voltage (V)
B	Square unipolar pulsed current	100	500	10	10	255	15	212
B1	Square unipolar pulsed current	100	1500	10	10	262	17	227
B2	Square unipolar pulsed current	100	500	20	10	247	18	192
B3	Direct current	100	—	—	10	145	5	110

shape. Unipolar pulsed current, used in PEO, generates alternating current to prevent electrode polarization by controlling electrical arcs. Using asymmetrical alternating current (unequal positive and negative amplitude), including unbalanced (dipole) pulse current, modified dipole pulse current, and alternating current (AC), provides further ability to control the coating process [15, 16].

There are a large number of studies on the investigation of the morphology of TiO2 coatings made by PEO on Ti substrates, but few have been performed on assessing their tribological properties. S. Aliasghar and et al. investigated the tribological performance of the titanium oxide coatings fabricated by PEB using a phosphate/silicate electrolyte with a frequency of 50 Hz and a duty cycle of 50-70%. They reported that the coatings were limited in thickness to ~40 to 50 μm and the coefficient of friction was 0.8 compared with ~0.5 for the untreated titanium [17]. In his study, we evaluated the effects of frequency, duty cycle, and applied current on the wear characteristics of nanocrystalline TiO2 coatings produced with PEO in a carbonate electrolyte with different frequencies and duty cycles.

2. Materials and Methods

Commercially pure (CP-grade II) titanium plates with dimensions of $13 \times 13 \times 3$ mm were used as the substrate, connected to the positive pole of the power supply as anode. The chemical analysis of the substrate was carried out by quantometer and the results are presented in Table 1. The plates were polished with 240, 400, 600, 800, 1000, and 1500 sandpapers and then with 0.5 μm Al_2O_3 powder. To remove organic contaminants from the samples' surfaces, they were immersed in a solution consisting of acetone, ethanol, and distilled water for 10 min in an ultrasonic bath. An ASTM 316 stainless steel cylindrical container, surrounding the substrates, was used as a cathode (negative pole). The coating solution consisted of 21.2 $g.L^{-1}$ sodium carbonate and 5 $g.L^{-1}$ sodium hydroxide. During the coating process, the electrolyte temperature was $25 \pm 2^{\circ}C$. Coating parameters are demonstrated in Table 2. The B, B1, and B2 samples were produced in square unipolar and at different frequencies and duty cycles, whereas the B3 coating was grown with direct current. As shown in this Table, the maximum electric power, the current density, and the processing time were constant for all the samples, i.e., 6 kW, 100 $mA.cm^{-2}$, and 10 min, respectively.

X-ray diffraction analysis (XRD, Philips, model PW-1730) with Cu-Kα radiation at a wavelength of 1.54 Å was employed to evaluate the coatings' phases. XRD was conducted at a scan rate of 0.05 deg/s, with an applied voltage of 40 kV and an electric current of 30 mA. The coatings' morphology was studied using scanning electron microscopy (SEM, LEO 435-VP) and field emission scanning electron microscopy (FESEM, TESCAN MU-Mira 3). Before placing the samples in the SEM device equipped with EDX, they were conductive with gold coating. The elemental compositions of coatings were evaluated by the energy dispersive X-ray spectroscopy (EDX) technique. Before the SEM and EDX analyses were performed, the samples were coated with Au to improve the conductivity. The surface topography of coatings was inspected through atomic force microscopy (AFM, Veeco auto probe) with a silicon pin of 10 nm tip in contact mode with air. The roughness of the layers was obtained by AFM and Proscan software (Ver. 1.7).

The coatings' wear characteristics, including friction coefficient, weight loss, and abrasion rate, were evaluated using a non-lubricated pin-on-disk wear test (TSN-WTC 02) at $25 \pm 2^{\circ}C$ with a humidity of 21%. The pin's applied load and speed were 2 N and 0.05 $m.s^{-1}$, respectively, and its sliding distance was 100 m. The samples had a circle shape with a 5 mm diameter. The pin was made of AISI-52100 steel with a length of 50 mm and a diameter of 2 mm. Wear analysis was conducted according to the ASTM G-99 standard.

3. Results and Discussion

3.1. Voltage-Time (V-T) Curve. According to the V-t curves of the samples (Figure 1), the voltage increased intensively in the region I, and the oxide film began to form. The

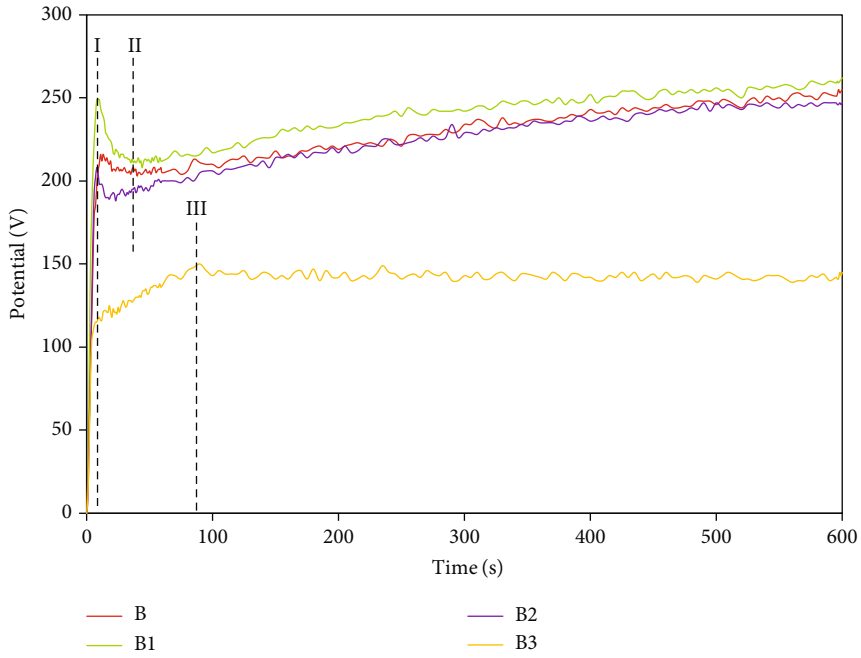

Figure 1: Voltage-time curve of coating process for the B, B1, B2, B3, and B4 samples.

anodizing process was first performed in this region to create a high-resistance dielectric protective layer on the surface. Increasing frequency in the B1 sample enhanced voltage, while voltage in the B2 sample was suppressed by increasing the duty cycle. In the B3 sample, voltage instantaneously increased, which might be because direct current (without a pulse) was used, and the current reached the breakdown zone [18]. The release of oxygen gas around the anode (Ti), corresponding to dielectric breakdown and plasma formation [15, 19], and an increase in voltage during the constant current density process, caused increased electrical resistance.

In the region II, in which the V-t curve follows Faraday's electrolysis laws, voltage was reduced by 6%, 15%, and 9% for the B, B1, and B2 samples, respectively. In this region, voltage decreased with a slight slope, indicating a breakdown of the protective film produced in region I. Reducing the slope in the region II could be because of the presence of ions and electrons, while the high-steep slope in region I was attributed to ionic current [20]. The difference between voltage and time was due to the increase of the input current and duty cycle for the B2 sample and the frequency difference for the B and B1 samples. This resulted in a dielectric breakdown and suppressed voltage. The sparking process occurred in region II, and the related information is shown in Table 2 for all samples. As shown in Figure 1 and Table 2, the direct current process is different from a unipolar pulsed current process. In region II, there was a dielectric breakdown at the beginning of the direct current process, resulting in a critical voltage. In this region, the voltage increases only occurred for the B3 sample since a voltage drop was observed for the unipolar pulsed current samples; in other words, voltage increased at a lower rate in the region. Also, the oxygen release rate was low in this region [21], and the acoustic emission activity somewhat stopped before reaching the breakdown voltage. In this step, the oxide layer's growth rate was reduced due to porosity formation [18]. In region III of the samples produced with unipolar pulsed current, the voltage increased slightly, and eventually the voltage and resistance became constant.

3.2. Phase Analysis. As demonstrated in the XRD patterns of the coated and non-coated titanium samples (Figure 2), titanium dioxide is composed of anatase and rutile. The generated heat on the anode surface caused by electrical sparks is the main factor in anatase and rutile fabrication. Figure 2 shows the highest amount of rutile was formed in layers that were grown in the direct current.

Despite using an electrolyte containing sodium, no sodium peak was detected in the XRD results, probably due to the decomposition of sodium carbonate and sodium hydroxide [22, 23].

The reason for the titanium peak in the XRD results is likely X-ray beam penetration through coatings [18]. Titanium, anatase, and rutile were detected in the B, B1, and B2 samples. The average temperature of metallic substrate holder was been reported about 400°C during the plasma electrolyte oxidation process [24, 25]. Anatase transforms irreversibly to rutile at elevated temperatures. The disparity in the intensity of rutile summits formed in the B sample compared with the B1 and B2 samples was due to the increase in the voltage level (as frequency was enhanced) and duty cycle (as voltage decreased). The weight percentages of oxides obtained from the XRD peak intensity were calculated using equations (1) and (2) [26, 27].

$$X_R = \frac{1}{1 + 0.8\,(I_A/I_R)} \quad (1)$$

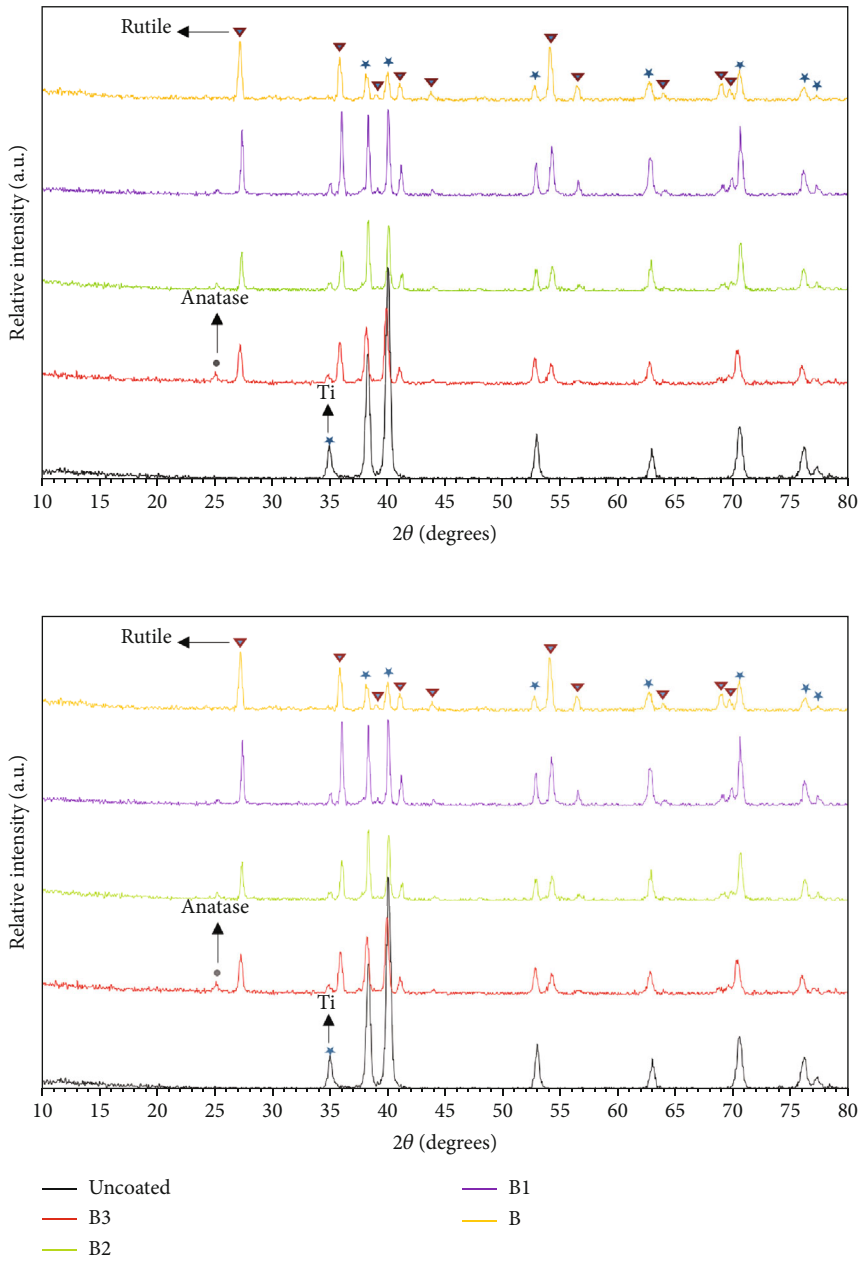

Figure 2: The X-ray diffraction patterns of the Ti substrate and coated B, B1, B2, and B3 samples.

$$X_A = 1 - X_R \text{ Or } X_A = \frac{1}{1 + 1.26\,(I_R/I_A)} \quad (2)$$

Where XR and XA are the weight percentage of the rutile and anatase phases and IR and IA are the peak intensities of anatase (101) and rutile (110) peaks, respectively. Table 2 demonstrates the weight percentages of the anatase, and rutile phases formed in the B, B1, B2, and B3 samples. In the B sample, the weight percentage was reduced from 22.2% to 3.66% in the anatase phase. At the same time, the weight percentage increased from 77.8% to 96.34% in the rutile phase. The transformation of anatase into a rutile phase (more thermodynamically stable) is most likely due to voltage and plasma intensity changes, directly affecting the micro-spark intensity and the oxide film's thermal gradient [15, 18, 24]. Table 2 presents the crystallographic properties of the B, B1, B2, and B3 samples. Although the XRD technique can estimate the crystal size with an acceptable tolerance, TEM and FESEM analyses have been suggested to measure more accurately the crystal size. The Debye-Scherrer equation (Eq. 34) was employed to calculate the crystal size (D) [26].

$$D = \frac{0.94\,\lambda}{\left(\beta_1^2 - \beta_\varepsilon^2\right)^{0.5}\cos\theta} \quad (3)$$

Where λ is the wavelength of the radiation beam (1.54041 Å), θ is the X-ray diffraction angle, β_1 is the peak

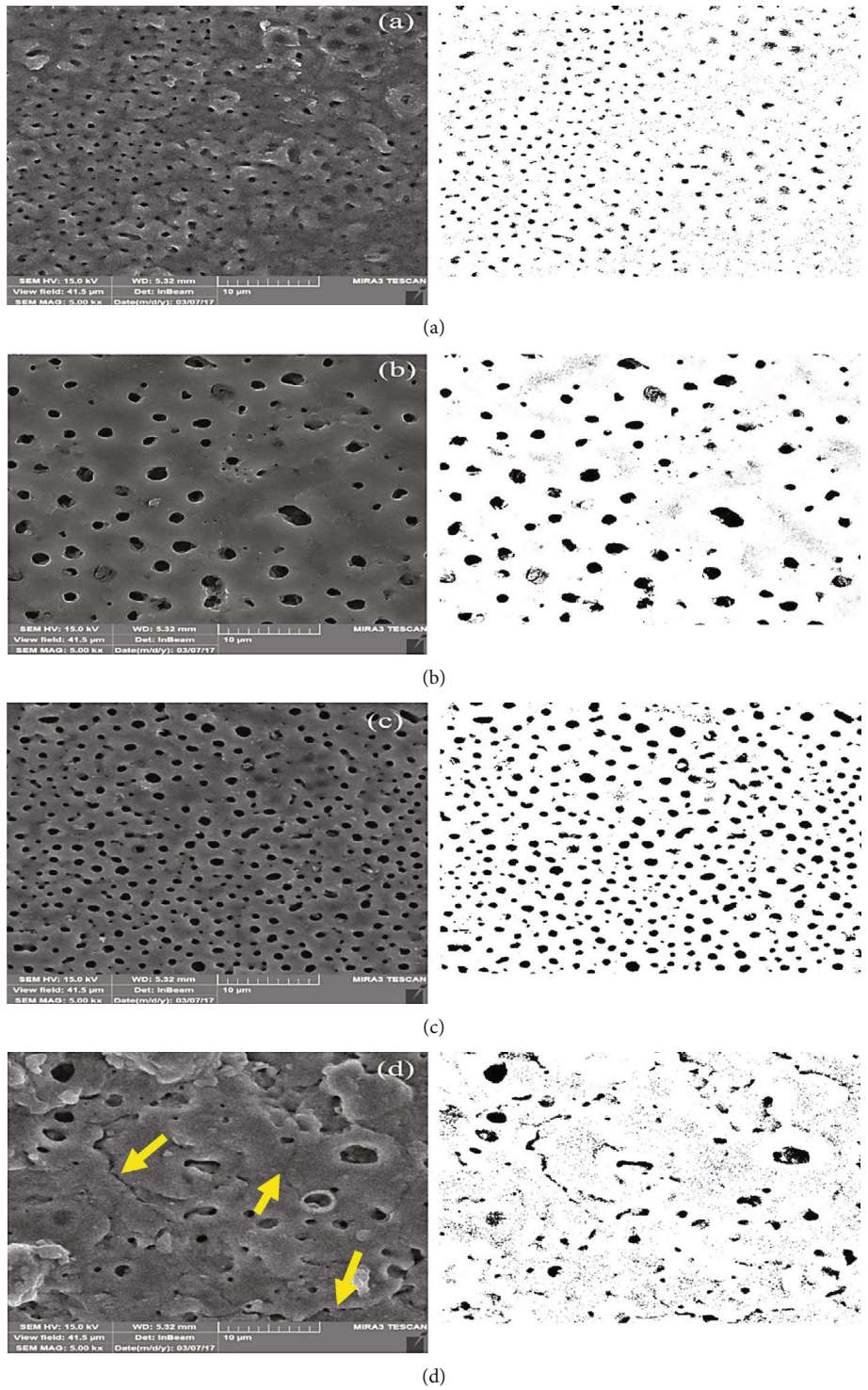

Figure 3: The SEM micrographs of (a) B, (b) B1, (c) B2, and (d) B3 samples.

width at half maximum, and β_ε is the peak broadening due to the micro-strain.

Average crystallite sizes in the B, B1, B2, and B3 samples were 40.5 nm, 29.5 nm, 48.3 nm, and 39 nm, respectively. It has been demonstrated that the TiO_2 nanocrystal-coated surface exhibits significant improvements in the tribological properties of titanium [27].

3.3. Microstructure and Topography Analysis. Figure 3 depicts the surface morphology of the coatings obtained using unipolar pulsed current and direct current. According to the voltage-time curve (Figure 1), voltage variations changed the average size of porosity in the coatings. The average diameter and volume fraction of porosity in the coatings were measured using the image analysis software (Table 2).

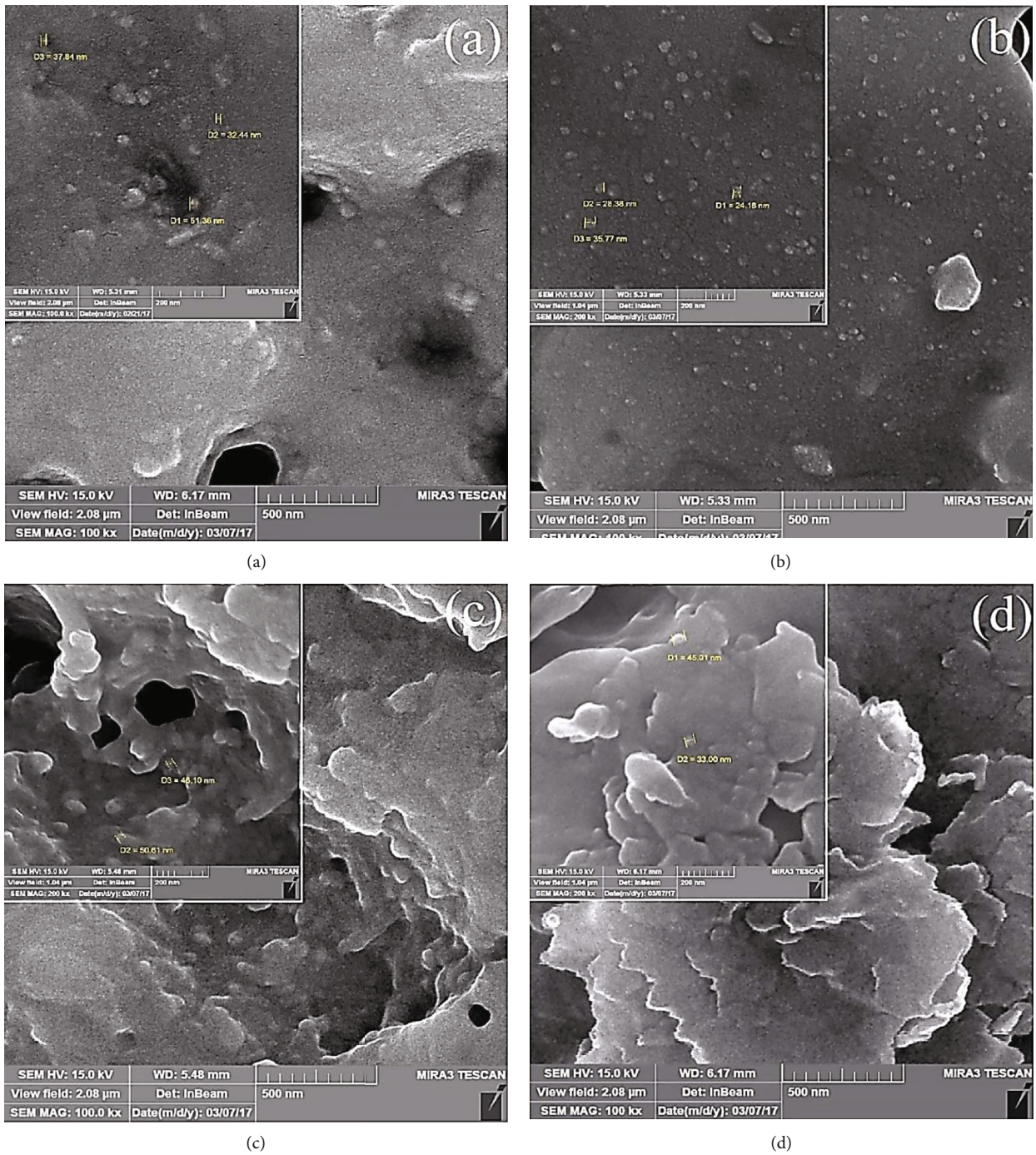

Figure 4: The FESEM micrographs of the (a) B, (b) B1, (c) B2, and (d) B3 samples.

The results revealed that porosities' diameters changed as the coating parameters varied. The B1 sample (coated with unipolar pulsed current, a duty cycle of 20%, and a frequency of 1000 Hz) showed the highest volume of porosity. The same sample was found to have the highest average diameter of porosity. It is worth noting that the applying higher voltages causes the passage of more electric current through the electrochemical cell due to more energetic electrical sparks. Such strong electrical avalanches lead to the formation of wider pores. In addition, the density of surface pores increases with increasing voltage. This is because when the voltage applied to the electrochemical cell increases, the anode voltage also increases, making it easier to reach the breakdown potential of the surface oxide layer and the gas layer that covers the anode. Consequently, more electron avalanches occur in the vicinity of the anode, leading to the formation of more pores [28].

Regarding Figure 3, the sample coated with unipolar pulsed current revealed a pancake microstructure with different pore sizes. A porous microstructure was observed in

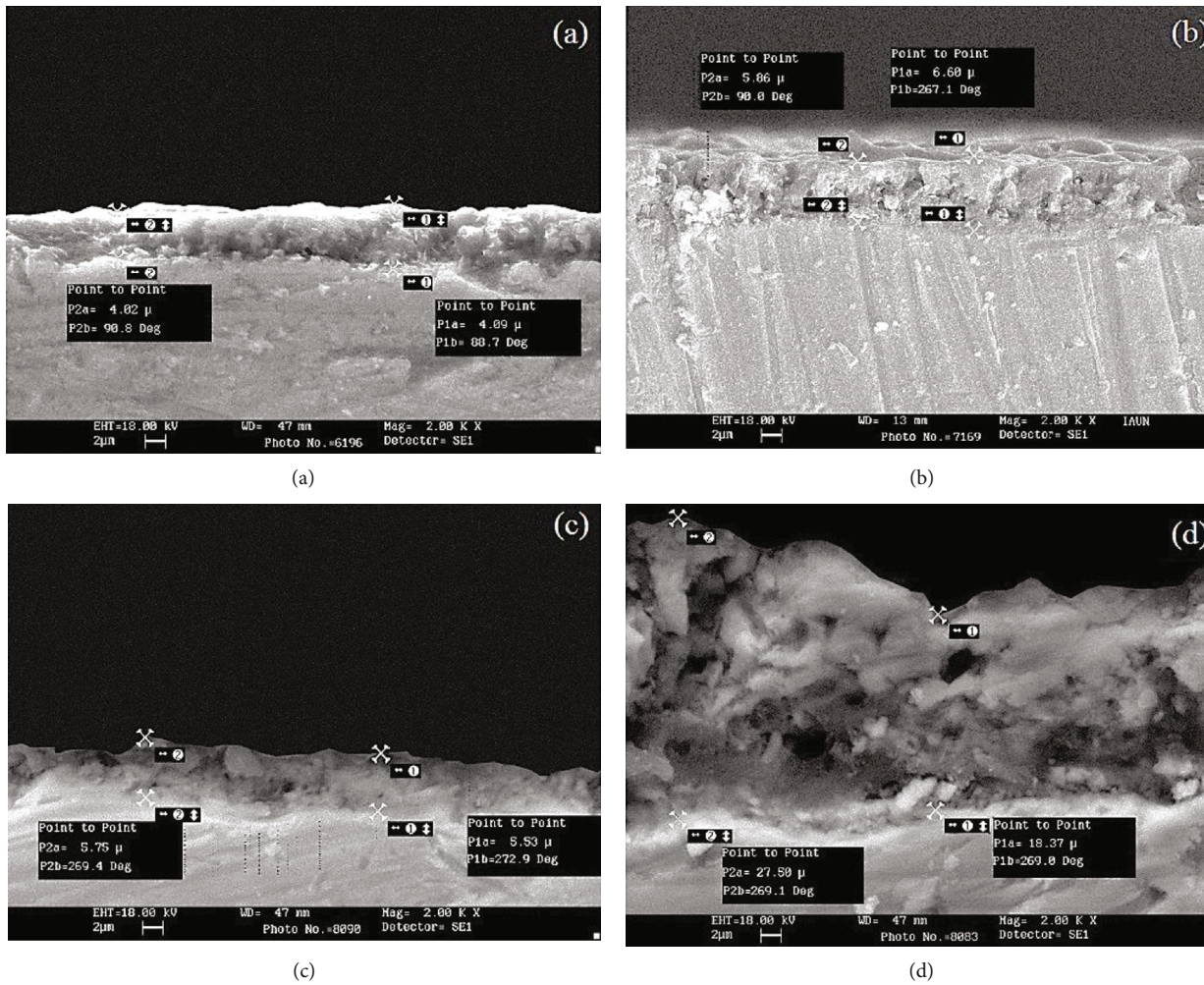

(a) (b) (c) (d)

Figure 5: The SEM cross-section micrographs of the (a) B, (b) B1, (c) B2, and (d) B3 samples.

all the coatings, with changing frequency, duty cycle, and current causing the coatings' microstructure to change. It was found that as frequency and voltage increased, surface roughness was enhanced (Figure 3(b)). Increasing frequency multiplied by the size and number of discharge channels resulted in a coating with a higher roughness [5]. As shown in Figure 3(c), increasing duty cycle raised the pores' diameter formed on the samples' surface and, consequently, enhanced surface roughness. Dark circular spots distributed in the SEM micrographs of the B3 sample were discharge channels developed during the coating process. Volcano-like microstructure formation affected the rapid solidification of the oxide products (TiO_2) and increased coating thickness near the discharge channels in the B3 sample. As discharge channels cooled down, reaction products were deposited on the channel walls. Then, the generated gases were stimulated to exit the channels, resulting in the formation of a volcano-like microstructure on the coating surface [27]. In Figure 3(d), the micro-cracks in the B3 coating were basically due to an increase in the electrical discharge power of direct current. Moreover, micro-cracks were produced with electrolytic plasma, probably due to the internal stress, contraction of the molten material produced with electrical discharge, and the difference between the phases produced in the outer and inner coatings. Another possible reason for the presence of micro-cracks in the B3 sample was the rapid cooling around the micro-sparks.

As rapid cooling occurred around the sparks' locations, the molten metal experienced a high contraction, ultimately forming surface micro-cracks [28, 29]. Thermal stress was caused by rapid solidification. In other words, the growing layer was melted due to surface electrical discharge, and it quickly solidified, resulting in micro-cracks on the surface. Moreover, some micro-cracks were observed on the B3 sample's surface, which might be due to increased heat produced by the sparks. In other words, higher energy in the direct current process resulted in more local melting of metal.

Figure 4 illustrates the surface morphology of the B, B1, B2, and B3 samples at various magnifications. As observed in this Figure, the samples had a crystalline microstructure. By increasing the frequency of the B1 sample, the voltage variation rate was enhanced, and the grains became smaller as they did not have enough time for growth. The size of the grains was also affected by temperature. Continuous micro-sparks at a lower frequency increased the local temperature, which enhanced the grain size [30]. In the B2

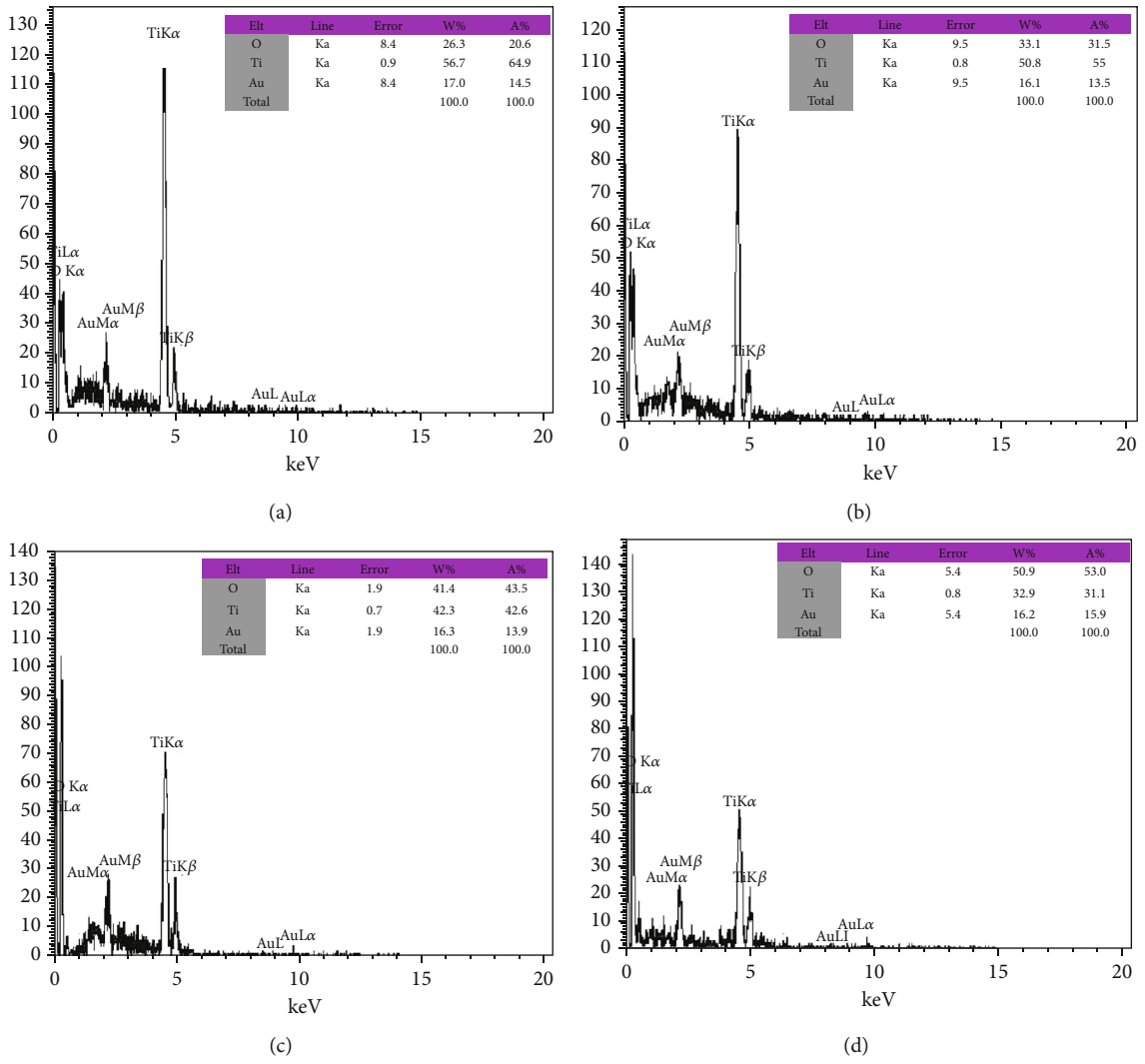

Figure 6: The EDS analysis of (a) B, (b) B1, (c) B2, and (d) B3 samples.

sample, increasing the duty cycle enhanced the final voltage, which increased the pulse's operation time and simplified the grains' growth during the time. The dielectric layer formed with electrical discharge during the coating process was stable in the coating obtained using direct current (B3). However, using unipolar pulsed current destabilized the layer, suppressing the grain growth rate. In the B3 sample, the substrate was exposed continuously to electrical discharge, and allowing more growing time for the grains.

As illustrated in Figure 5, the B, B1, B2, and B3 samples had a thickness of $4.0 \pm 0.74\,\mu$m, $6.2 \pm 0.95\,\mu$m, $3.6 \pm 0.71\,\mu$m, and $23 \pm 1.4\,\mu$m, respectively. Also, all samples produced with unipolar pulsed current revealed dense coatings with good adhesion to the substrate, unlike B3. Moreover, it was found that the B1 sample thickness was enhanced by increasing frequency. This fact is also evidenced in published studies [31, 32]. It can be stated that the micro-discharge generated by thermal ionization lasted longer and transformed a greater mass on the substrate. Therefore, in direct current, it resulted in a thicker coating. However, in unipolar pulsed current, it causes an intense micro-discharge with a low plasma lifetime.

Figure 6 depicts the coating's chemical composition measured using EDS. Oxygen and titanium were observed in all the coatings. It should be noted that the presence of Au was due to the coating procedures before EDS analysis. Based on the atomic percentage of titanium and oxygen detected by EDS analysis, the main constituent phase is supposed to be titanium oxide. By increasing the applied voltage and electric field in the B1 sample compared to the B sample, the amount of oxygen increased in the TiO_2 coating of the Ti anode increased [33].

As shown in Table 3, based on the surface topography of the layer synthesized at various times on a scale of $3\,\mu$m $\times 3\,\mu$m the average surface roughness numbers (Ra) of the layers grown in different conditions. It is foreseeable that after the sparks disappear, the melted areas are frozen around the electrolyte and a rough layer is formed. By comparing the B3 sample with coatings produced using unipolar pulsed current, it was found that the B3 coating had greater roughness,

Table 3: Phase and microstructural characteristics of the coatings.

Sample	Anatase (Wt. %)	Rutile (Wt. %)	Average porosity size (μm)	Porosity volume fraction (vol. %)	Average surface roughness (μm)
B	5.45	94.55	0.64	8.12	0.33
B1	3.66	96.34	2.07	9.73	0.44
B2	12.02	78.98	0.98	10.54	0.36
B3	22.2	77.80	2.31	6.86	2.00

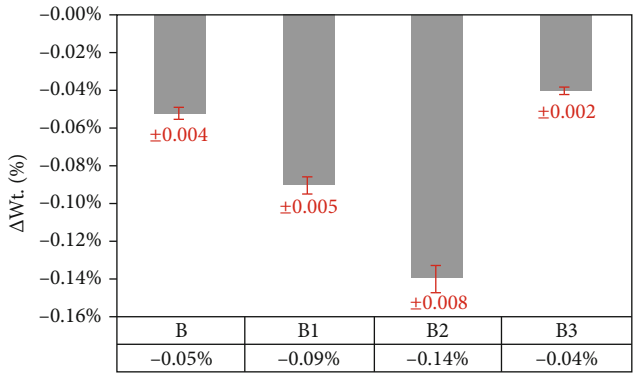

Figure 7: Weight changes of the samples (wt. %) in the wear test.

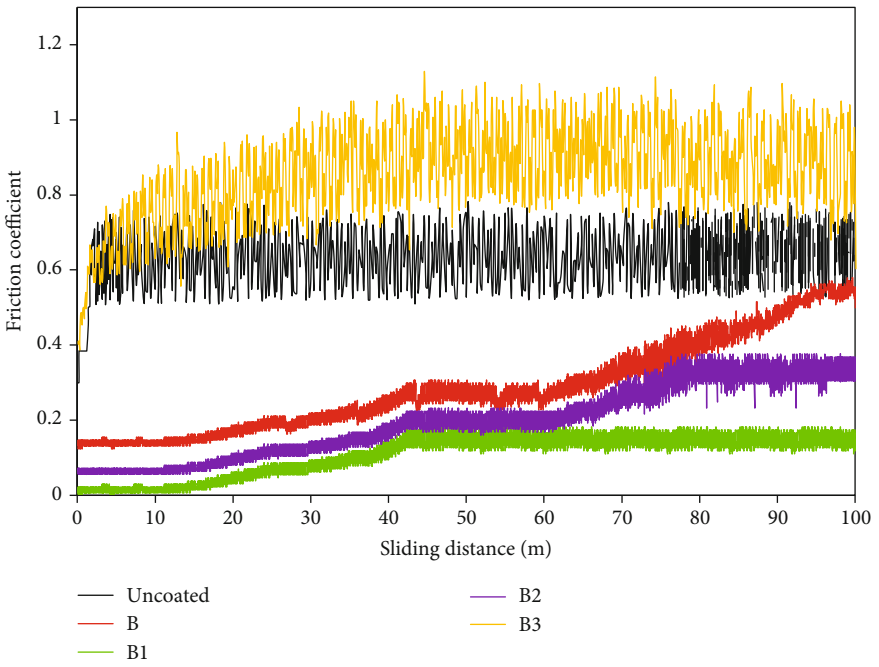

Figure 8: Friction coefficient versus the sliding distance for the Ti substrate and B, B1, B2, and B3 samples.

which are most likely due to the strong electric field and dielectric breakdown during the coating process [34, 35].

PEO coatings' roughness typically depends on the substrate's surface roughness and coating parameters [15]. It is known that sparks' lifetime in the PEO coating process increases by enhancing frequency, and longer sparks' lifetime leads to larger particle sizes. In other words, coatings can increase surface roughness as the spark channels increase in diameter. With a greater duty cycle, less time is needed between two pulses. The molten material is solidified at the interval between two pulses; thus, as this time is reduced, the material does not have enough time to crystalize and becomes amorphous [15]. This results in increasing the amount of porosity and surface roughness in coatings.

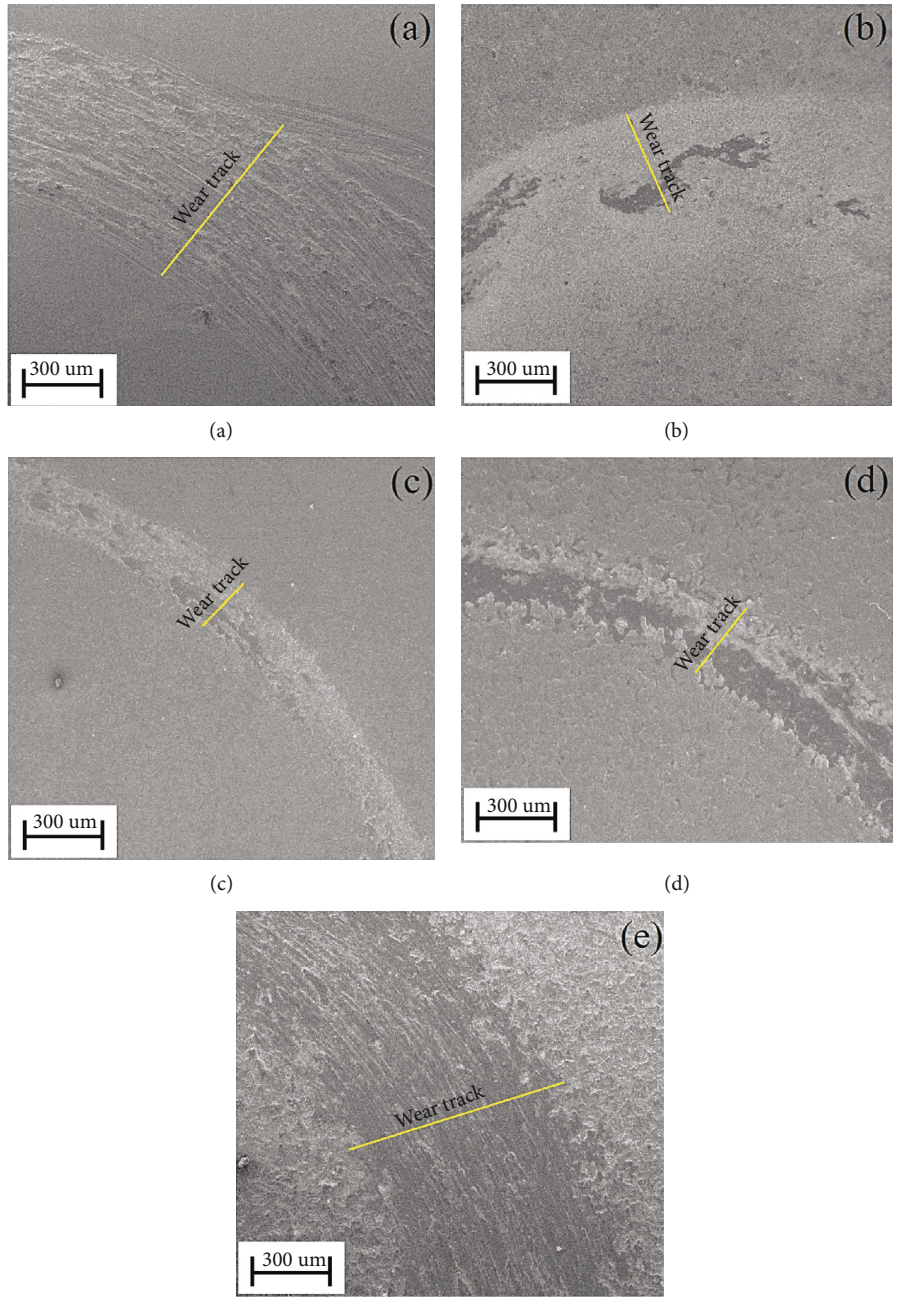

Figure 9: The SEM micrographs of (a) Ti substrate, (b) B, (c) B1, (d) B2, and (e) B3 samples after the wear test.

3.4. Tribological Behavior. As illustrated in Figure 7, the B3 sample (coated using direct current) had the lowest weight loss, whereas the highest weight loss was found in the B2 sample (coated using unipolar pulsed current at the frequency of 500 Hz). The massive difference in weight loss among samples coated with unipolar pulsed current is probably due to incomplete coating formation, low thickness, and high porosity in the coatings. As a result, as the coating forms on the substrate, electric resistance increases and power and the number of electrical discharges is reduced, and thus, coating growth continues at a prolonged rate. The difference in weight loss among samples coated with direct current and unipolar pulsed current was due to the higher deposition rate [14].

$$\%\Delta W = \frac{M_2 - M_1}{M_2} \times 100 \quad (4)$$

Where M_1 is the sample's weight before coating, M_2 is the sample's weight after coating, and ΔW is the percentage of weight change. During the coating process, the substrate

may dissolve, which results in weight loss. Additionally, as the substrate is coated, it gains weight. Therefore, weight loss and weight gain determined the samples' final weight (Equation (4)).

After the coating process, the samples' weights were reduced, indicating that the weight of the formed coating was lower than that of the dissolved substrate.

Figure 8 depicts the friction coefficients of the coated and uncoated samples. The adhesion and detachment of abrasive particles causes the friction coefficient to oscillate, causing the force between the abrasive surface and the coating to fluctuate. Based on the friction between the abrasive body and TiO_2 coating surfaces, the friction coefficient increased up to 0.5 from the beginning to 40 m sliding distance due to the oxide layer's loss and the high roughness of the coating surface. Due to further contact between the pin and the coating surface, the friction coefficient showed a decreasing trend at 0-40 m and then reached a constant value for the coated samples up to 100 m. The B1 sample showed better tribological behavior as the high density and good adhesion of the coating to the substrate increased the wear resistance between the pin and the titanium oxide coating surface. The friction coefficient of the B3 sample reached 0.85 after 45 m sliding distance and remained constant up to the sliding distance of 100 m. For the B3 sample, a steep slope at the beginning of the test might be attributed to the rapid increase in the number of abrasion particles between the two surfaces, which increased the wear rate. Typically, the friction coefficient becomes stable when the number of abrasive particles between surfaces is equal to the number of abrasive particles removed from wear surfaces [36, 37].

Figure 9 demonstrates the SEM images of the uncoated and coated samples after the wear test. The wear mechanism for the uncoated titanium was a combination of adhesion and abrasion, which might be due to plastic deformation on the coating surface and the abrasion between the pin and the coating during the wear test. No surface fracture was detected in this Figure and only some micro-cracks were observed, showing the presence of the abrasive wear mechanism [36, 37]. Some white spots were observed on the coatings' surface after the wear test, indicating the adhesion mechanism.

4. Conclusions

The PEO process was used with sodium carbonate electrolyte to coat titanium oxide on a pure titanium substrate, with a current density of 825 mA/cm^2, various frequencies and duty cycles, and different types of current. The following results were obtained from this research study:

(1) Samples coated using 1500 Hz-10%-267 V and 1500 Hz-10%-145 V revealed the highest and lowest potential, respectively

(2) The phase analysis results showed that the sample coated with direct current had a uniform rutile phase. The sample coated with unipolar pulsed current had a relatively small amount of the anatase phase in addition to the rutile phase

(3) A pancake microstructure was revealed by samples coated using unipolar pulsed current. Increasing frequency enhanced the porosity size compared to samples obtained with unipolar pulsed current. The coatings produced with direct current had a volcano-like microstructure with some micro-cracks on the coating surface

(4) The B3 sample (which used direct current) revealed the highest roughness and thickness, while the B1 sample (which used unipolar pulsed current) had the lowest roughness and thickness

(5) After 100 m sliding distance, the wear test results depicted that the friction coefficient of samples coated using unipolar pulsed current was reduced and wear resistance improved significantly. However, samples coated using direct current showed more wear resistance than the unipolar pulsed current samples

(6) The XRD results showed a uniform titanium oxide and rutile phase

Data Availability

Data available on request.

Conflicts of Interest

The author(s) declare(s) that they have no conflicts of interest.

References

[1] S. G. Lim and H. C. Choe, "Bioactive apatite formation on PEO-treated Ti-6Al-4V alloy after 3rd anodic titanium oxidation," *Applied Surface Science*, vol. 484, pp. 365–373, 2019.

[2] J. Han, Y. Cheng, W. Tu, T. Zhan, and Y. Cheng, "The black and white coatings on Ti-6Al-4V alloy or pure titanium by plasma electrolytic oxidation in concentrated silicate electrolyte," *Applied Surface Science*, vol. 428, pp. 684–697, 2018.

[3] M. Laveissière, H. Cerda, J. Roche, L. Cassayre, and L. Arurault, "In-depth study of the influence of electrolyte composition on coatings prepared by plasma electrolytic oxidation of TA6V alloy," *Surface and Coatings Technology*, vol. 361, pp. 50–62, 2019.

[4] W. Liu, Y. Liu, Y. Lin, Z. Zhang, and T. Shi, "Effects of graphene on structure and corrosion resistance of plasma electrolytic oxidation coatings formed on D16T Al alloy," *Applied Surface Science*, vol. 475, pp. 645–659, 2019.

[5] M. Kaur and K. Singh, "Review on titanium and titanium based alloys as biomaterials for Orthopaedic applications," *Materials Science and Engineering: C*, vol. 102, pp. 844–862, 2019.

[6] L. Chen, X. Jin, Y. Qu et al., "High temperature tribological behavior of microarc oxidation film on Ti-39Nb-6Zr alloy," *Surface and Coatings Technology*, vol. 347, pp. 29–37, 2018.

[7] N. Ao, D. Liu, X. Zhang, and C. Liu, "Enhanced fatigue performance of modified plasma electrolytic oxidation coated Ti-6Al-4V alloy: effect of residual stress and gradient nanostructure," *Applied Surface Science*, vol. 489, pp. 595–607, 2019.

[8] A. Bordbar-Khiabani, S. Ebrahimi, and B. Yarmand, "*Highly Corrosion Protection Properties of Plasma Electrolytic Oxidized Titanium Using rGO Nanosheets*," *Applied Surface Science*, vol. 486, pp. 153–165, 2019.

[9] S. Abbasi, M. R. Bilesan, and F. Golestani-Fard, "In vitro evaluation of the biocompatibility and bioactivity of plasma electrolyte oxidized titania/calcium phosphate nanocoatings on Ti," *Journal of Materials Science*, vol. 54, no. 5, pp. 4277–4286, 2019.

[10] R. Cai, C. Zhao, and X. Nie, "Effect of plasma electrolytic oxidation process on surface characteristics and Tribological behavior," *Surface and Coatings Technology*, vol. 375, pp. 824–832, 2019.

[11] G. Mortazavi, J. Jiang, and E. I. Meletis, "Investigation of the plasma electrolytic oxidation mechanism of titanium," *Applied Surface Science*, vol. 488, pp. 370–382, 2019.

[12] W. Liu, C. Blawert, M. L. Zheludkevich et al., "Effects of graphene Nanosheets on the ceramic coatings formed on Ti6Al4V alloy drill pipe by plasma electrolytic oxidation," *Journal of Alloys and Compounds*, vol. 789, pp. 996–1007, 2019.

[13] F. Samanipour, M. R. Bayati, F. Golestani-Fard et al., "Innovative fabrication of ZrO_2-HAp- TiO_2 nano/micro-structured composites through MAO/EPD combined method," *Materials Letters*, vol. 65, no. 5, pp. 926–928, 2011.

[14] F. Golestani-fard, M. R. Bayati, H. R. Zargar, S. Abbasi, and H. R. Rezaei, "MAO-preparation of nanocrystalline hydroxyapatite-titania composite films: Formation stages and effect of the growth time," *Materials Research Bulletin*, vol. 46, no. 12, pp. 2422–2426, 2011.

[15] N. Ao, D. Liu, X. Zhang, K. Fan, and C. Liu, "The effect of residual stress and gradient nanostructure on the fretting fatigue behavior of plasma electrolytic oxidation coated Ti-6Al-4V alloy," *Journal of Alloys and Compounds*, vol. 811, article 152017, 2019.

[16] A. Santos-Coquillat, R. Gonzalez Tenorio, M. Mohedano, E. Martinez-Campos, R. Arrabal, and E. Matykina, "Tailoring of antibacterial and osteogenic properties of Ti6Al4V by plasma electrolytic oxidation," *Applied Surface Science*, vol. 454, pp. 157–172, 2018.

[17] S. Aliasghar, P. Skeldon, and G. E. Thompson, "Plasma electrolytic oxidation of titanium in a phosphate/silicate electrolyte and tribological performance of the coatings," *Applied Surface Science*, vol. 316, pp. 463–476, 2014.

[18] S. Abbasi, F. Golestani-Fard, S. M. M. Mirhosseini, A. Ziaee, and M. Mehrjoo, "Effect of electrolyte concentration on microstructure and properties of micro arc oxidized hydroxyapatite/titania nanostructured composite," *Materials Science and Engineering: C*, vol. 33, no. 5, pp. 2555–2561, 2013.

[19] Y. Gao, A. Yerokhin, E. Parfenov, and A. Matthews, "Application of voltage pulse transient analysis during plasma electrolytic oxidation for assessment of characteristics and corrosion behaviour of ca- and P-containing coatings on magnesium," *Electrochimica Acta*, vol. 149, pp. 218–230, 2014.

[20] S. Sarbishei, M. A. Faghihisani, and M. R. Mohammadi, "Effects of alumina nanoparticles concentration on microstructure and corrosion behavior of coatings formed on titanium substrate via PEO process," *Ceramics International*, vol. 42, no. 7, pp. 8789–8797, 2016.

[21] S. Abbasi, M. R. Bayati, F. Golestani-Fard et al., "Micro arc oxidized HAp-TiO_2 nanostructured hybrid layers-part I: Effect of voltage and growth time," *Applied Surface Science*, vol. 257, no. 14, pp. 5944–5949, 2011.

[22] Y. Han, S. H. Hong, and K. Xu, "Structure and in vitro bioactivity of titania-based films by micro-arc oxidation," *Surface and Coatings Technology*, vol. 168, no. 2-3, pp. 249–258, 2003.

[23] W. Xiaohong, J. Zhaohua, L. Huiling, X. Shigang, and H. Xinguo, "Photo-catalytic activity of titanium dioxide thin films prepared by micro- plasma oxidation method," *Thin Solid Films*, vol. 441, no. 1-2, pp. 130–134, 2003.

[24] M. R. Bayati, A. Z. Moshfegh, and F. Golestani-Fard, "Effect of electrical parameters on morphology, chemical composition, and photoactivity of the nano-porous titania layers synthesized by pulse-microarc oxidation," *Electrochimica Acta*, vol. 55, no. 8, pp. 2760–2766, 2010.

[25] K. Venkateswarlu, N. Rameshbabua, D. Sreekanth, A. C. Bose, V. Muthupandi, and S. Subramanian, "Fabrication and characterization of micro-arc oxidized fluoride containing Titania films on Cp Ti," *Ceramics International*, vol. 39, no. 1, pp. 801–812, 2013.

[26] K. Venkateswarlu, N. Rameshbabua, D. Sreekanth et al., "Role of electrolyte additives on _in-vitro_ electrochemical behavior of micro arc oxidized titania films on Cp Ti," *Applied Surface Science*, vol. 258, no. 18, pp. 6853–6863, 2012.

[27] A. Amanov, S. Sasaki, D. E. Kim, O. V. Penkov, and Y. S. Pyun, "Improvement of the tribological properties of Al6061-T6 alloy under dry sliding conditions," *Tribology International*, vol. 64, pp. 24–32, 2013.

[28] S. Abbasi, F. Golestani-Fard, H. R. Rezaie, S. M. M. Mirhosseini, and A. Ziaee, "MAO-derived hydroxyapatite-TiO_2 nanostructured bio- ceramic films on titanium," *Materials Research Bulletin*, vol. 47, no. 11, pp. 3407–3412, 2012.

[29] J. A. Curran and T. W. Clyne, "Thermo-physical properties of plasma electrolytic oxide coatings on aluminium," *Surface and Coatings Technology*, vol. 199, no. 2-3, pp. 168–176, 2005.

[30] A. Bahramian, K. Raeissi, and A. Hakimizad, "An investigation of the characteristics of Al_2O_3/TiO_2 PEO nanocomposite coating," *Applied Surface Science*, vol. 351, pp. 13–26, 2015.

[31] H. Khanmohammadi, S. R. Allahkaram, N. Towhidi, and A. M. Rashidfarokhi, "Preparation of PEO coating on Ti_6Al_4V in different electrolytes and evaluation of its properties," *Surface Engineering*, vol. 32, no. 6, pp. 448–456, 2016.

[32] X. Liang, Z. Liu, and B. Wang, "State-of-the-art of surface integrity induced by tool wear effects in machining process of titanium and nickel alloys: A review," *Measurement*, vol. 132, pp. 150–181, 2019.

[33] L. P. Qiao, J. Lou, S. F. Zhang, B. Qu, W. H. Chang, and R. F. Zhang, "The entrance mechanism of calcium and phosphorus elements into micro arc oxidation coatings developed on Ti_6Al_4V alloy," *Surface and Coatings Technology*, vol. 285, pp. 187–196, 2016.

[34] P. Bala Srinivasan, J. Liang, R. G. Balajeee, C. Blawert, M. Stormer, and W. Dietzel, "Effect of pulse frequency on the microstructure, phase composition and corrosion performance of a phosphate-based plasma electrolytic oxidation coated AM50 magnesium alloy," *Applied Surface Science*, vol. 256, no. 12, pp. 3928–3935, 2010.

[35] S. Abbasi, F. Golestani-Fard, H. R. Rezaie, and S. M. M. Mirhosseini, "MAO-derived hydroxyapatite/TiO_2 nanostructured multi- layer coatings on titanium substrate," *Applied Surface Science*, vol. 261, pp. 37–42, 2012.

[36] Q. Xia, D. Zhang, D. Li, Z. Jiang, and Z. Yao, "Preparation of the plasma electrolytic oxidation coating on Mg![single bond](https://sdfestaticassets-eu-west-1.sciencedirectassets.-com/shared- assets/55/entities/sbnd.gif)Li alloy and its thermal control performance," *Surface and Coatings Technology*, vol. 369, pp. 252–256, 2019.

[37] S. Tsunekawa, Y. Aoki, and H. Habazaki, "Two-step plasma electrolytic oxidation of Ti-15V-3Al-3Cr-3Sn for wear- resistant and adhesive coating," *Surface and Coatings Technology*, vol. 205, no. 19, pp. 4732–4740, 2011.